Supplementary Information

Quantum Dot-Conjugated SARS-CoV-2 Spike Pseudo-Virions Enable Tracking of Angiotensin Converting Enzyme 2 Binding and Endocytosis

Kirill Gorshkov[1,*], Kimihiro Susumu[2,3], Jiji Chen[4], Miao Xu[1], Manisha Pradhan[1], Wei Zhu[1], Xin Hu[1], Joyce C. Breger[5], Mason Wolak[2], Eunkeu Oh[2,*]

Supplementary Discussion

As described in the Results and Discussion section, we have developed and optimized QD-Spike protein conjugates that enable a wide range of biochemical and cellular assays that allow for detailed investigation of Spike/ACE2 interactions and intracellular compartmentalization and trafficking. The QD-Spike conjugates also allow us to study the inhibition of these processes and conduct high-throughput screening of entire libraries of drugs to identify inhibitors of the initial receptor binding event. Furthermore, the conjugates have the potential to be used for specific cellular drug delivery given the high affinity binding and internalization that is a prominent characteristic of these nanoparticle probes.

Biochemical Assays

We initially focused on developing the requisite chemistry to attach Spike protein subunits to fluorescent QDs in an effort to generate a SARS-CoV-2 analog that could be monitored either *in vitro* or *in vivo* by the condition-dependent presence or absence of light emitted from the QD. Three separate QD formulations were prepared with carefully engineered PL emission λ_{max} (514 nm, 528 nm, and 608 nm) in order to establish a library of QDs that might be suitable for use under different high-content imaging conditions in cellular assays. The expected molecular activity between Spike/ACE2 (binding) and Spike/ACE2/antibodies (inhibition of binding) was confirmed before moving on to high-content imaging of QD-Spike interactions with live HEK293T cells stably transfected with ACE2-GFP.

QD-Spike conjugates were stabilized in solution by addition of BSA and borate buffer to reduce aggregation and non-specific binding, and to prevent dissolution. Optimized biochemical assays showed roughly 80% maximum efficiency. The TEM images of complexed QD-Spike RBD:AuNP-

ACE2 revealed that AuNPs tended to be clustered together, which may cause additional quenching because of the inner screening effect of AuNP or self-quenching of QD.[1] Regardless of the fit to the individual models, the observed PL quenching indicated that binding between the Spike protein subunit and ACE2, demonstrating that attachment of Spike proteins to QD is a viable method for the production of pseudo-virions that can be monitored, potentially in real time, by their emission characteristics. Biochemical inhibition assays using two different neutralizing antibodies (Ab1 and Ab2) showed EC_{50} = 60 nM and 125 nM, respectively. While the immunogens used to develop the neutralizing antibodies were the S1 subunit for Ab1, and the RBD for Ab2, Ab1 was more potent than Ab2. These results indicated that our pseudo-virions can enable facile and rapid biochemical screening of inhibition for repurposed or newly synthesized drug targets in addition to neutralizing antibodies or other biologics.

Cellular Assays

High-content imaging qualitatively confirmed that the binding affinity between the Spike RBD and ACE2 is extremely high,[2] as the Spike RBD:ACE2 [endo(RBD:ACE2)] complex persisted throughout endocytosis and internalization. Furthermore, we demonstrated that the SARS-CoV-2 RBD alone was enough to induce the endocytosis of ACE2. This was previously demonstrated for SARS-CoV-1 in ACE2-GFP HEK293 cells[3] with recombinant protein, an experiment that was replicated with recombinant Spike RBD in this work.

The cell-based assays in this work were initially developed using HEK293T cells stably transfected with ACE2 receptors tagged with GFP, and the cells were treated with pseudo-virions comprising either QD_{514} or QD_{608} bound to 8 units of Spike RBD, or QD_{528} with 3 units of S1+S2 ECD . Importantly RBD-facilitated QD uptake was not observed in cells without ACE2 expression, highlighting the importance of ACE2 in viral infection. While the pseudo-virions were able to bind and internalization, emission from both QD_{514} and QD_{528} bled through into the channel used to image the ACE2-GFP receptors (λ_{max} = 509 nm). Consequently, QD_{608}-RBD was chosen for all experiments moving forward because the QD_{608}-RBD conjugates could be easily differentiated from the ACE2-GFP receptors, which was critical for monitoring early timepoints during spatiotemporal experiments. Such experiments show rapid binding of the QD_{608}-RBD conjugates to ACE2-GFP within 10 min of treatment, and QD_{608}-RBD and ACE2-GFP were colocalized at the plasma membrane with significant internalization being observed within 20 min. Nearly full internalization was achieved within 3 h, with the signal being compartmentalized to the peri-nuclear region. While this was a surrogate assay for viral infection, one can imagine that the live-virus infection kinetics are rapid as well once the cell recognizes the virus *via* the ACE2 receptor. At this time point, the signal from the QD_{608}-Spike RBD is very tightly clustered into puncta that are likely endosomes following endocytosis. This was confirmed when no QD_{608} emission was observed from the cytoplasm after treatment of cells with Dyngo-4a, a known endocytosis blocker *via* dynamin inhibition.[4] The current high-content experiment and analysis did not allow us to fully differentiate membrane spots *versus* endocytosed spots with 100% accuracy. Nonetheless, the endocytosis experiments reveal dramatic differences in Spot Counts, and this was confirmed with visual inspection.

We demonstrated through further high-content cellular imaging that biologics such as recombinant protein and neutralizing antibodies acted as very potent inhibitors of the viral Spike protein. Low nanomolar EC_{50} concentrations of 8.4 nM and 49 nM were measured for Ab1 and Ab2, respectively. It should be noted that in biochemical inhibition assays, the efficacy of the antibodies followed the same trend, with lower EC_{50}s for Ab1 than Ab2. Biochemical inhibition assays did show relatively higher EC_{50}s than did cell-based assays; this may be due to the possible contribution of non-specific binding of antibody to AuNPs in solution and other QD PL quenching such as the inner screening effect of AuNP, or electron transfer between NPs. Extrapolating to live virus infection assays, our data supports the idea that the biologics bind the Spike protein on the surface of the viral particle, preventing its recognition by the ACE2 receptor, and blocking the downstream effects such as membrane fusion and viral endocytosis. The research also suggests that QD_{608}-RBD conjugates could potentially be used to identify other host cell receptors that utilize SARS-CoV-2 binding and internalization to initiate infection,[5] further demonstrating their versatility.

Future work involving advanced human airway epithelial tissue models[6] will allow us to probe the spatiotemporal dynamics of Spike-ACE2 interactions in a more application-specific manner. It is interesting that the cell line used often in the literature as a standard for respiratory viral infection was found in our experiment to stain moderately for the ACE2 receptor. However, it must be noted that normal lung tissue is known to have moderate to low levels of ACE2 expression.[7-9] Instead the mRNA of the protein is found highly expressed in heart, kidney, and testes.[7-9] However, for a virus to get to these tissues it must be get into the body, and the fact that it is indeed an airborne virus that preferentially enters through the nasal epithelium and presents with such severe respiratory problems suggests that there may be enough ACE2 in the lungs to cause infection, or that those that get infected somehow have higher ACE2 in the lungs to begin with. We believe it has been well-demonstrated that there are co-morbidities with COVID-19, and some of those have been found to be COPD, as well as smoking, which are thought to increase ACE2 expression and make those individuals more susceptible.[10] Children, as it turns out, have even lower levels of ACE2 expression, and this may account for the fewer number of cases and generally lower case severity in the youthful population.[10] The inclusion of the Calu-3 cell line was intended to demonstrate this idea that a low amount of ACE2 can still make a cell permissive to SARS-CoV-2 infection, and we believe our QD pseudo-virions demonstrate this well.

Altogether, we have effectively established a platform technology not only for this SARS-CoV-2 viral pandemic, but also future viruses that have an ACE2-mediated cell recognition and entry as the first step in viral infection. Importantly, our QD_{608}-RBD conjugates should enable high-throughput screening of inhibition effects because they can be resolved using high-content imaging at concentrations as low 5 nM in 1536 well plates. Consequently, we plan on screening currently available FDA-approved drug libraries using 1536 well plates to identify existing drugs that block Spike RBD internalization, and may therefore be repurposed for treatment of COVID-19. We further postulate that the QD_{608}-RBD conjugates may act as highly specific and potent delivery vehicles for drugs and other molecules of therapeutic interest directly to cells expressing ACE2 on the cell surface. This approach is feasible given the inherently low cytotoxicity of QD-RBD conjugates, and may be applied to not only coronavirus related pathogens, but to any virus that targets ACE2. Using an approach similar to that outlined here, we may be able to visualize intracellular inhibition using drugs delivered with our QD_{608}-RBD conjugates, opening the door for yet another application of these pseudo-virion nanoparticles.

Supplementary Methods

Energy transfer models.

To analyze the energy transfer efficiency of complexed QD-RBD:AuNP-ACE2, we considered three theoretical models.[11] FRET (dipole-dipole Förster resonance energy transfer) is based on dipole-dipole interaction.[12] Surface damping of the donor near metal surface, NSET (Nano-surface energy transfer) following a $1/R^4$ dependence, involves the excitation of electron-hole pairs in the metal surface, and volume damping of the donor near metal acceptor NVET (Nano-volume energy transfer), which follows a $1/(R^3 l)$ dependence (l = electron mean free path), where the energy is dissipated by conversion of electronic currents in the metal into heat through scattering from phonons, impurities, and other electrons.[13,14]

Energy transfer efficiency, E, and damping rate, k_{ET} (or energy transfer rate), can be described by the general expressions;

$$E = \frac{Nk_{ET}}{k_{D0} + Nk_{ET}} = \frac{N}{N + (\frac{R_0}{R})^X} \qquad (2)$$

$$k_{ET} = k_{D0} \, (\frac{R_0}{R})^X \qquad (3)$$

where $X = 4$ for surface damping (NSET), and $X = 3$ for volume damping (NVET). In this general equation, $X = 6$ can be referred for FRET. In the FRET model, R is defined as the AuNP-center to QD-center distance; for NSET and NVET models, R is defined as the distance from AuNP-surface to QD-center. The separation distance at which energy transfer efficiency equals 50%, R_0, for each model was described in a previous publication.[11]

For FRET, R_0 can be calculated from the donor luminescence and acceptor absorption data using the following equation:

$$R_0(\text{nm}) = (\frac{9 \ln 10 \, \kappa^2 \Phi_D^0}{128 \, \pi^5 n^4 N_{Av}} \times 10^{17} J)^{1/6} = (8.79 \times 10^{-11} \, \kappa^2 \, \text{n}^{-4} \Phi_D^0 J)^{1/6} \qquad (4)$$

where n is the refractive index of the buffer medium, N_{Av} is Avogadro’s number (6.022×10^{23} mol^{-1}),

$\Phi_D{}^0$ is the donor quantum yield in the absence of acceptor, κ^2 is the dipole orientation factor, and J is the spectral overlap integral function between donor emission and acceptor absorption. We use a κ^2 of 2/3, which is appropriate for the random dipole orientations of donor and acceptor found within these self-assembled configurations.[15,16] J is determined by integrating the acceptor absorbance $\varepsilon_A(\lambda)$ multiplied by the normalized donor luminescence $f_D(\lambda)$ over all wavelengths, λ.

$$J = \int_0^\infty J(\lambda)\mathrm{d}\lambda = \int_0^\infty f_D(\lambda)\varepsilon_A(\lambda)\lambda^4\mathrm{d}\lambda \qquad (5)$$

Here, $f_D(\lambda)$ is in nm^{-1}, $\varepsilon_A(\lambda)$ in M^{-1}cm^{-1}, and λ in nm, then J is in M^{-1}cm^{-1}nm^4 and R_0 (in nm).

Similar to R_0, the separation distances corresponding to 50% energy transfer efficiency can be derived for both surface and volume damping processes. For surface damping, R_0 corresponding to the separation distance at which energy transfer efficiency equals 50%, was calculated by using equation 6 based on the previous publication.[11,17]

$$R_0(Surface\ damping) = (0.225\frac{C^3\Phi_D^0}{\omega_D^2\,\omega_F\,k_F})^{1/4} \qquad (6)$$

where c is the speed of light in vacuum and $\Phi_D{}^0$ is the fluorescence quantum yield of the donor in the absence of acceptor. By analogy, we derive R_0 for volume damping:

$$R_0(Volume\ damping) = (0.563\frac{C^3\Phi_D^0}{\omega_D^2\,\omega_F\ k_F\,l_{Cor}})^{1/3} \qquad (7)$$

where $\qquad l_{Cor} = \left(\frac{2l_0\,l_{eff}}{l_0 + l_{eff}}\right)$

Here, l_0 and l_{eff} are the mean free path of the electrons in bulk metal and the effective mean free path in NPs when the size of NPs is smaller than l_0, respectively. Thus l_{Cor} is the corrected mean free path of the electrons in metal NPs, which we calculated as 7.6 nm for 5.6 nm AuNP used here. Based on equation 4,6, and 7, the calculated R_0 in our system is 13.9 nm for FRET, 6.5 nm for NSET and 8.4 nm for NVET in the case of QD$_{514}$-RBD and AuNP-ACE2.

Supplementary Figures

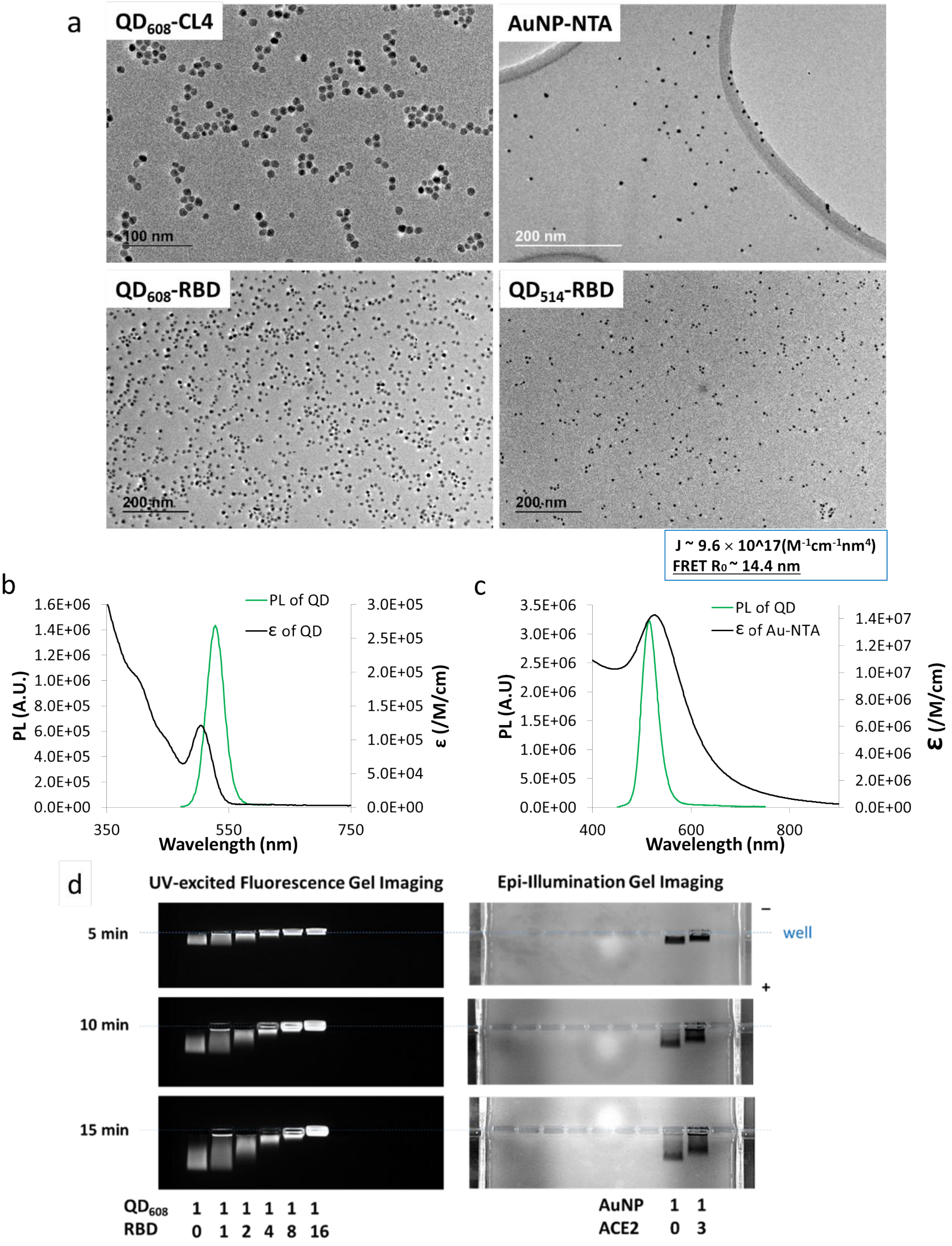

Supplementary Figure 1. Characterization of QD-RBD and AuNP probes. **a,** Top: TEM image of NPs with ligand only; QD608-CL4 (10.0 ± 0.93) nm and AuNP-NTA (5.6 ± 0.7 nm). Bottom: Low magnification TEM image of QDs conjugated with histidine-tagged RBD (RBD/QD =8); QD_{608}-RBD (10.1 ± 0.89 nm) and QD_{514}-RBD (8.2 ± 0.72 nm). **b,** Optical properties of QD_{528}. **c,** The emission spectrum of QD_{514} and its integral overlap with absorption spectrum of AuNP, with calculated *J* and

R_0 values. **d,** Gel electrophoresis of NPs with and without protein at different running times. Left: QD_{608}-CL4 with different conjugation ratios of histidine-tagged RBD protein. Right: AuNP-NTA and its conjugate AuNP-ACE2 with 3 molar excess of histidine-tagged ACE2.

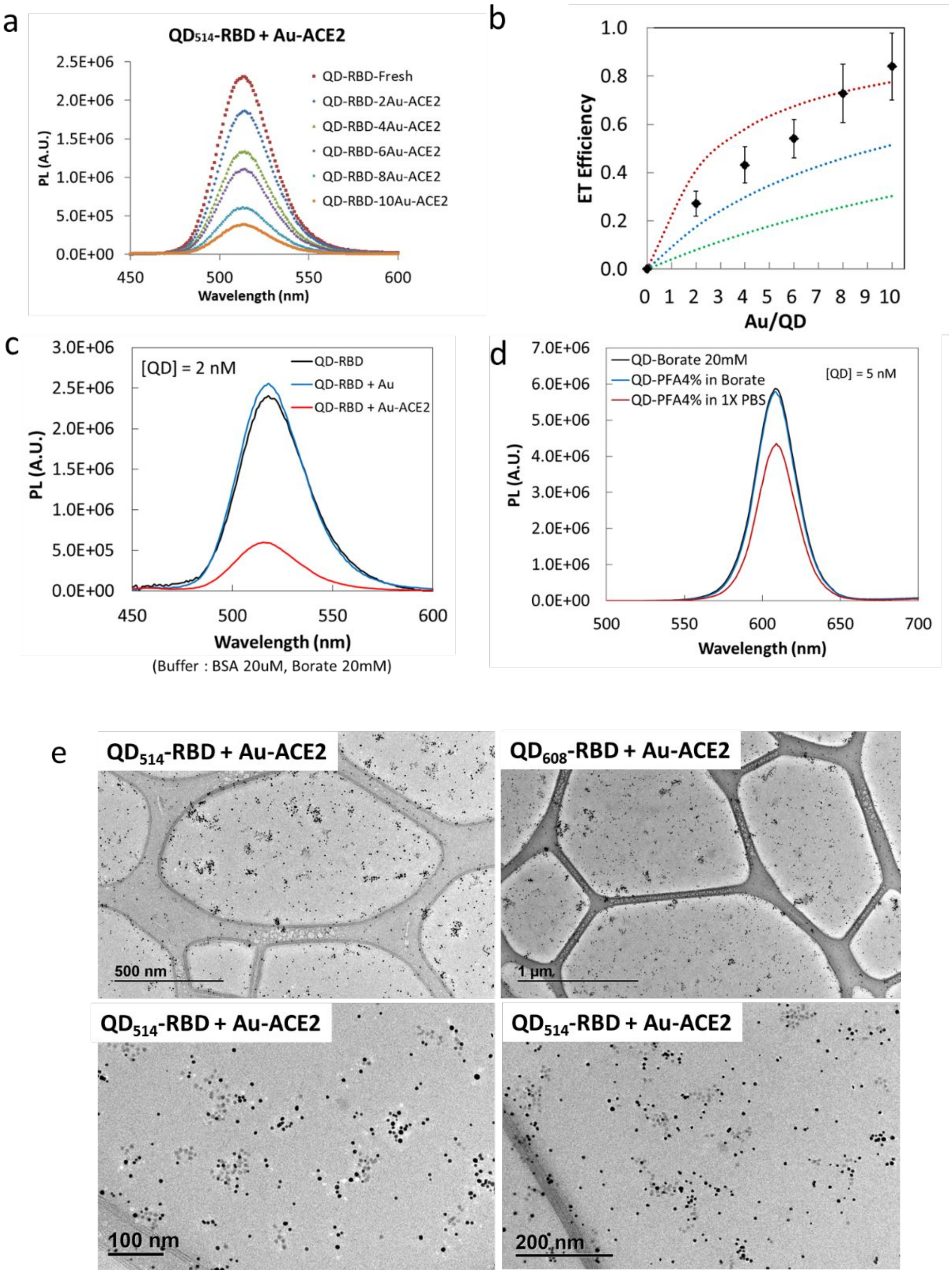

Supplementary Figure 2. Energy transfer experiment with different QDs and AuNPs. **a,** PL quenching of QD$_{514}$-RBD with smaller AuNP$_3$ (3 nm in diameter) with ACE2. **b,** Energy transfer efficiency of QD$_{528}$-S1 and AuNP-ACE2 with different ratio compared to the models. Here QD$_{528}$ was 4.1 nm in diameter. **c,** PL of QD$_{514}$-RBD, with and without AuNP. There was no QD PL quenching with AuNP-NTA (‘QD$_{514}$-RBD + Au’, blue line) but 70% quenching with AuNP-ACE2 conjugate (‘QD$_{514}$-RBD + Au-ACE2’) in the presence of 20μM BSA in borate buffer. **d,** QD$_{608}$ stability test with different buffer. **e,** TEM images of QD-RBD interaction with AuNP-ACE2. Top: low magnification images of QD$_{514}$-RBD with Au-ACE2 and QD$_{608}$-RBD with Au-ACE2. Bottom: representative TEM images of QD$_{514}$-RBD with Au-ACE2 with high magnification. Darker NPs were AuNP and lighter NPs were QDs.

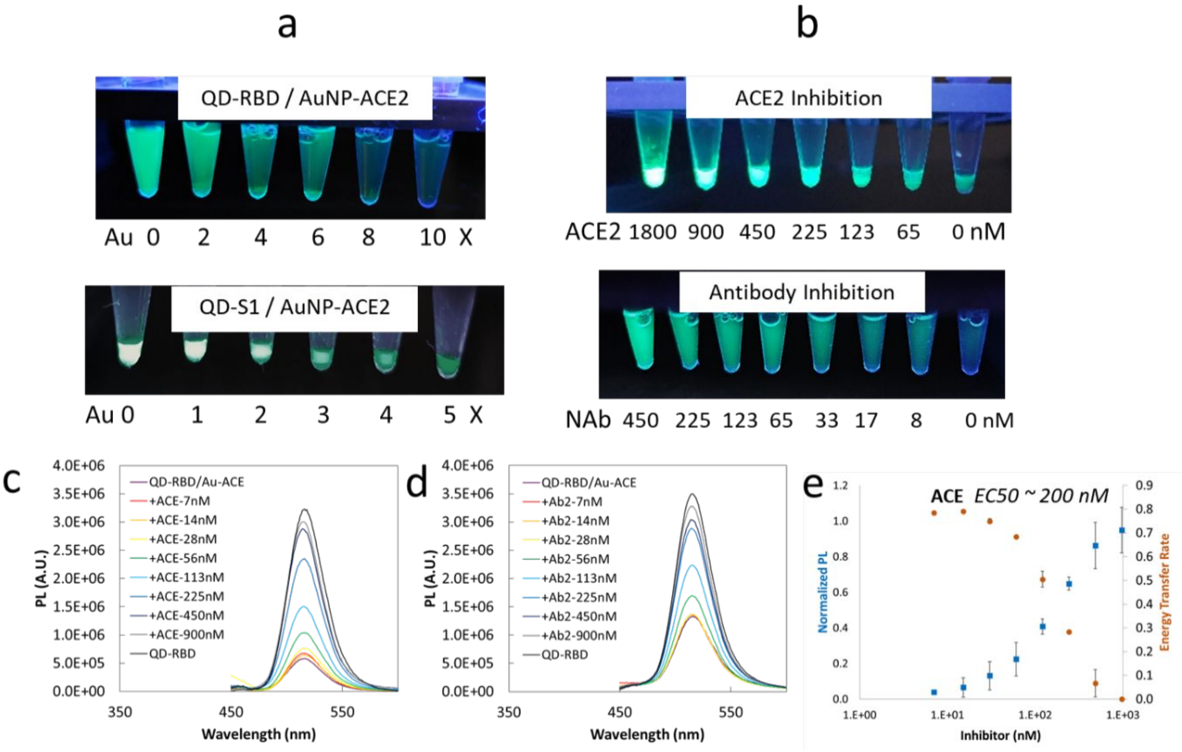

Supplementary Figure 3. Energy transfer assay and inhibition assay. **a**, Colloidal PL image of energy transfer experiment with different QDs and AuNPs; PL of QD$_{514}$-RBD with AuNP-ACE2 (top) and of QD$_{514}$-S1 (bottom) with different ratios of AuNP per QD; QD$_{514}$-S1 exhibited 20-30% lower quenching than QD$_{514}$-RBD with the same condition because the large size of S1 resulted in a larger separation between QD and AuNP. **b**, Colloidal PL image of inhibition study with different inhibitors using QD$_{514}$-RBD and AuNP-ACE2; QD PL increased with increasing amounts of Fc-tagged ACE2 inhibitor (top) and neutralizing antibody (bottom). **c.** Representative data of the ACE2-Fc inhibition assay using QD$_{514}$-RBD and AuNP-ACE2. **d**, Representative data of Ab2 inhibition assay using QD$_{514}$-RBD and AuNP-ACE2. **e.** The normalized PL of QD$_{514}$ and the calculated energy transfer efficiency. The EC$_{50}$ of Fc-tagged ACE2 was 200 nM with $R^2 > 99$ %.

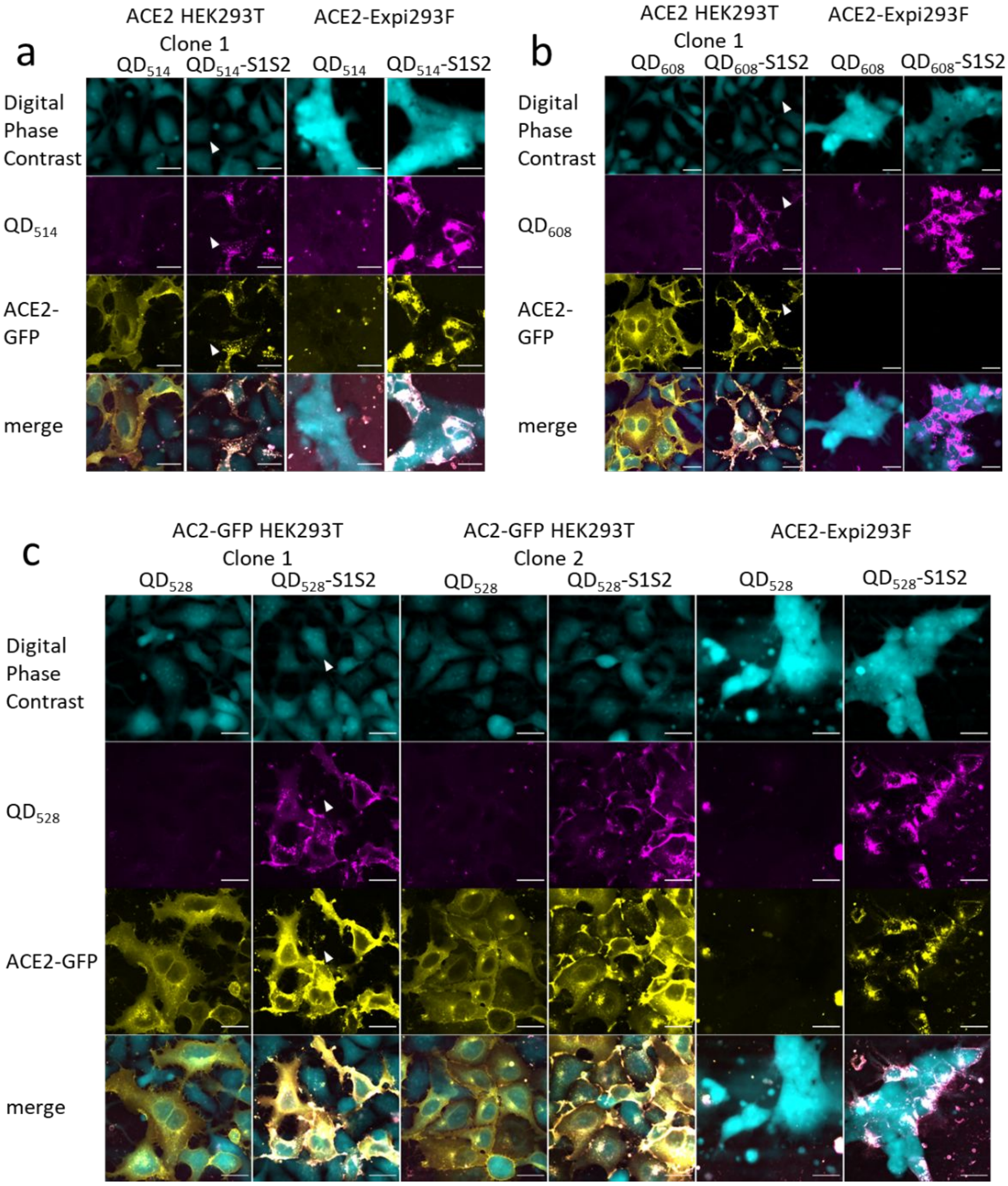

Supplementary Figure 4. QD-RBD induces translocation of ACE2 and internalizes into cells. **a,** Representative image montage of ACE2-GFP HEK293T clone 1, and untagged ACE2-Expi293F treated with 100 nM QD_{514}-RBD (magenta). Digital phase contrast (cyan) was used during live-cell imaging to identify cell bodies. The ACE2-GFP is represented by a yellow look-up table. In this case, the signal from QD_{514}-RBD bleeds through into the ACE2-GFP channel. Scale bar, 25 µm. White arrows demonstrate untransfected cells with no QD signal. **b,** Representative image montage of ACE2-GFP HEK293T clone 1 and ACE2-Expi293F treated with 100 nM QD_{608}-RBD (magenta). Digital phase contrast (cyan) was used during live-cell imaging to identify cell bodies. The ACE2-GFP is represented by a yellow look-up table. Scale bar, 25 µm. **c,** Representative image montage of ACE2-GFP HEK293T clone 1, ACE2-GFP HEK293T clone 2 and ACE2-Expi293F treated with 100 nM QD_{528}-S1S2 ECD (magenta). Digital phase contrast (cyan) was used during live-cell imaging to identify cell bodies. The ACE2-GFP is represented by a yellow look-up table. In this case, the signal from QD_{528}-S1S2 ECD bleeds through into the ACE2-GFP channel. Scale bar, 25 µm. White arrows demonstrate untransfected cells with no QD signal.

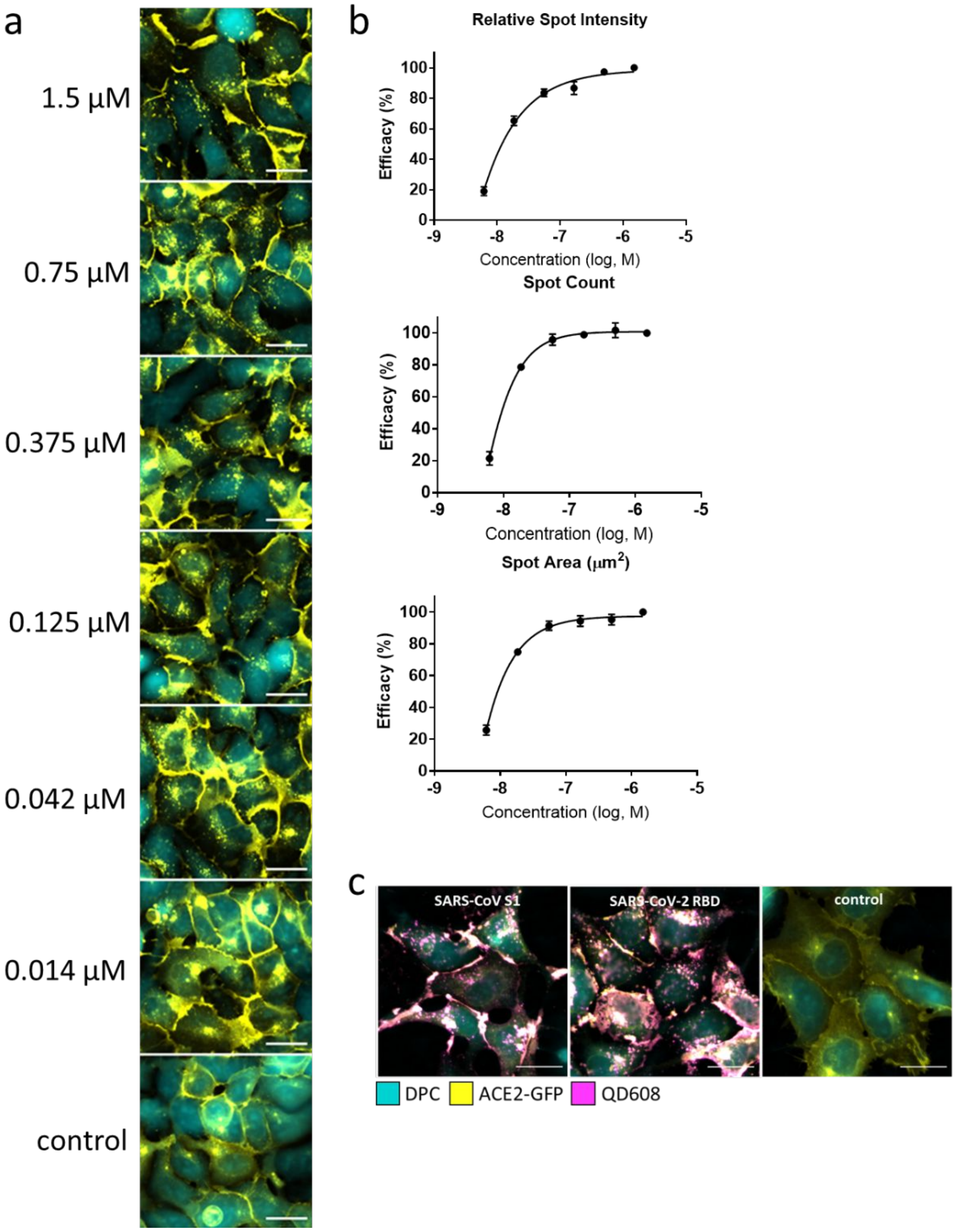

Supplementary Figure 5. Recombinant SARS-CoV-2 RBD can internalize into cells and induce ACE2-GFP translocation. **a,** Representative images of ACE2-GFP (yellow) HEK293T clone 2 treated with SARS-CoV-2 RBD from 1.5 µM to 0.014 µm. Digital phase contrast (cyan) was used during live-cell imaging to identify cell bodies. **b,** High-content measurements of Relative Spot Intensity, Spot Count, and Spot Area (µm^2) from cells in a. N = >3000 cells per well from three wells. **c,** Representative images of ACE2-GFP HEK293T clone 2 treated with 20 nM QD$_{608}$-SARS-CoV S1 and SARS-CoV-2 RBD (magenta). Digital phase contrast (cyan) was used during live-cell imaging to identify cell bodies. Scale bar, 25 µm. N = 10 fields each from triplicate wells.

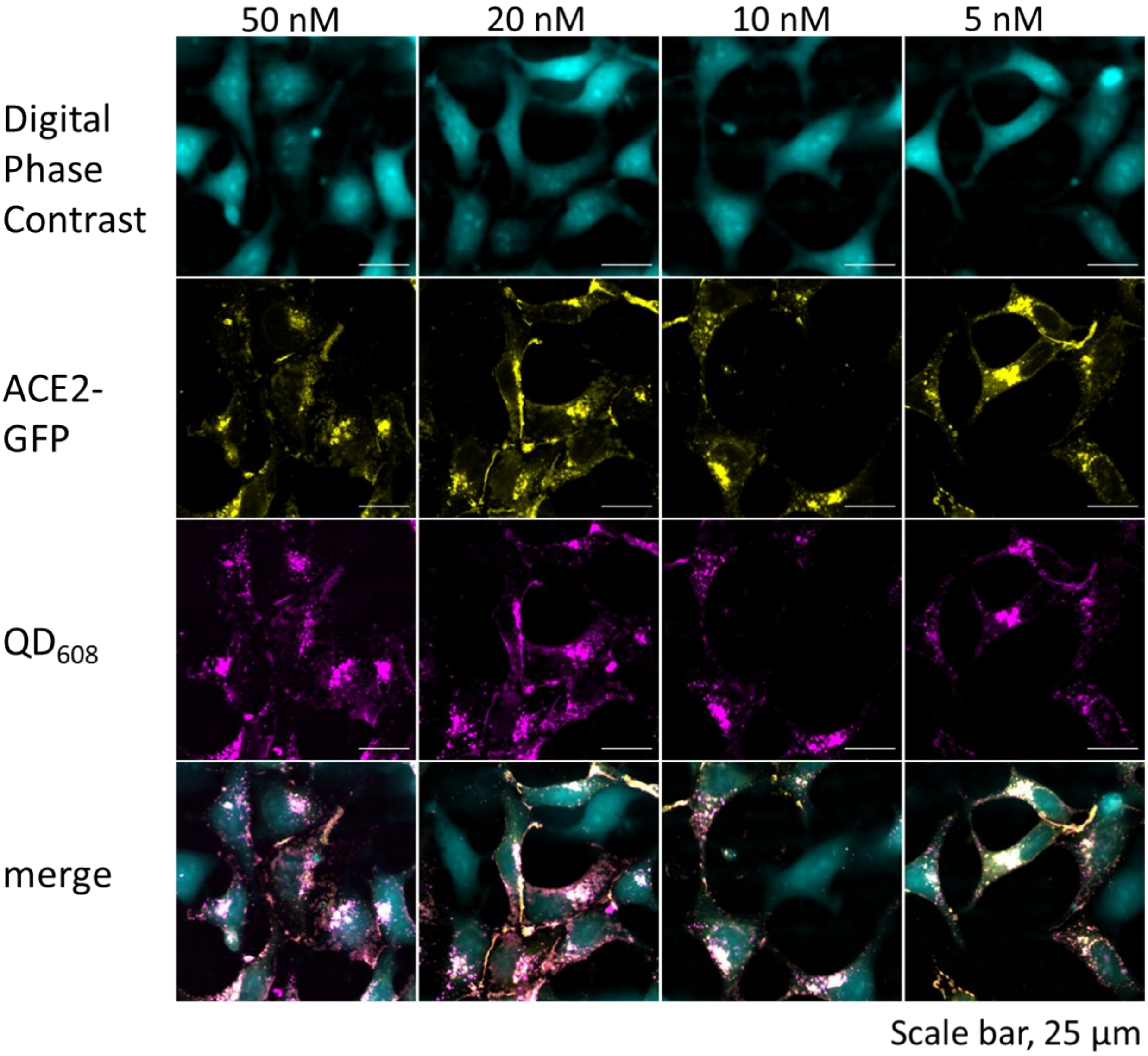

Supplementary Figure 6. QD_{608}-RBD can be traced even at low concentrations. Representative images of ACE2-GFP (yellow) HEK293T clone 2 treated with 50 nM to 5 nM QD_{608}-RBD (magenta). Digital phase contrast (cyan) was used during live-cell imaging to identify cell bodies. Scale bar, 25 µm. N = 10 fields each from triplicate wells.

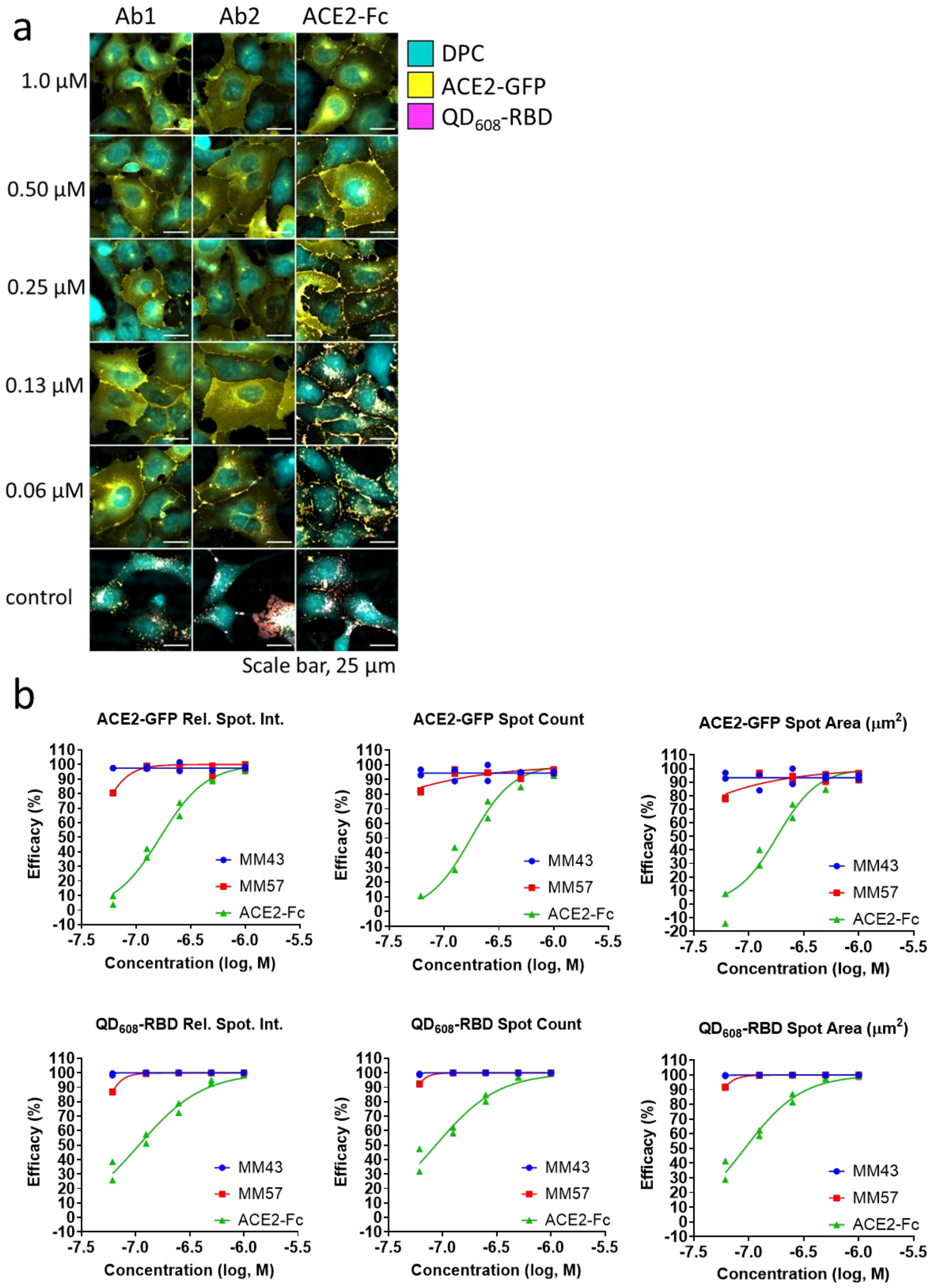

Supplementary Figure 7. QD_{608}-RBD can be inhibited by neutralizing antibodies and ACE2-Fc. **a,** Representative images of ACE2-GFP (yellow) HEK293T clone 2 treated with 10 nM QD_{608}-RBD (magenta) + Ab1 neutralizing antibody, Ab2 neutralizing antibody or rhACE2-Fc starting at 1.0 µM. Digital phase contrast (cyan) was used during live-cell imaging to identify cell bodies. Scale bar, 25 µm. **b,** Quantification of endo(RBD:ACE2) cells in **(a).** N = ~1200 cells in 8 fields from duplicate wells.

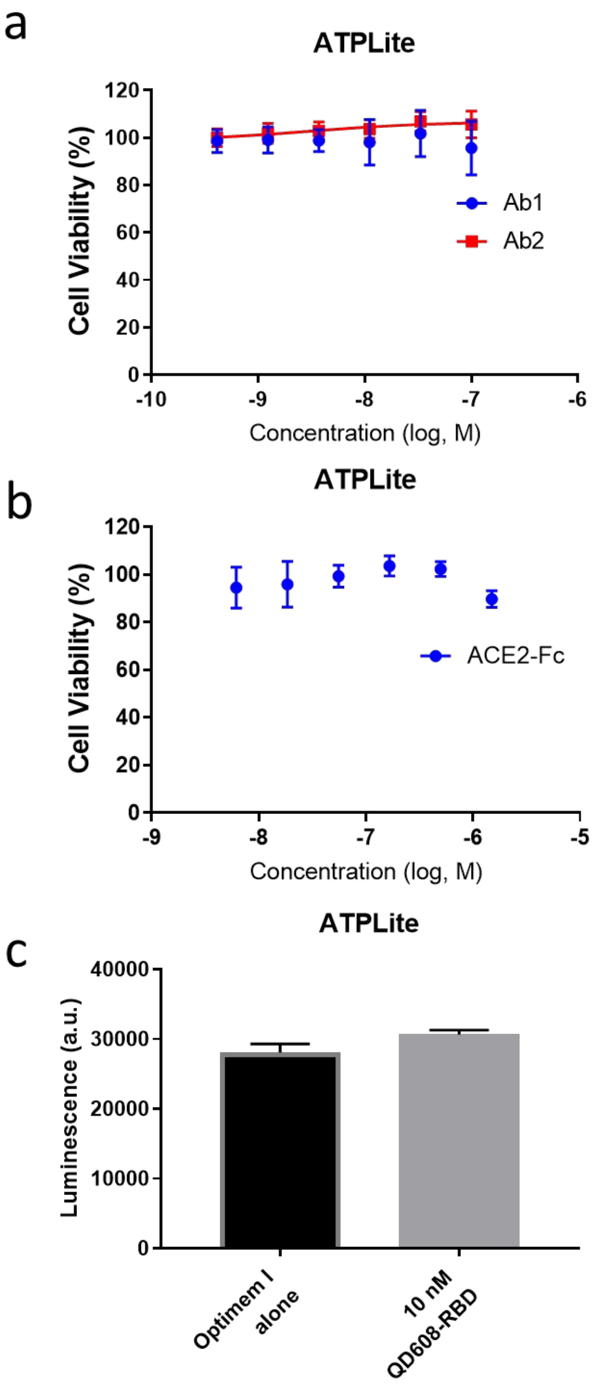

Supplementary Figure 8. QD$_{608}$-RBD did not decrease cell viability as measured by ATPLite. **a,** ATPLite cell viability concentration-response curves of ACE2-GFP HEK293T clone 2 treated with 10 nM QD$_{608}$-RBD + Ab1 neutralizing antibody (blue), Ab2 neutralizing antibody (red). **b,** ATPLite cell viability concentration-response curves of ACE2-GFP HEK293T clone 2 treated with 10 nM QD$_{608}$-RBD + ACE2-Fc starting at 1.0 µM. **(C)** ATPLite luminescence readings from cells treated with Optimem I alone or 10 nM QD608-RBD for 3 h. Error bars indicate S.D. N = 9 wells per condition from 3 independent experiments.

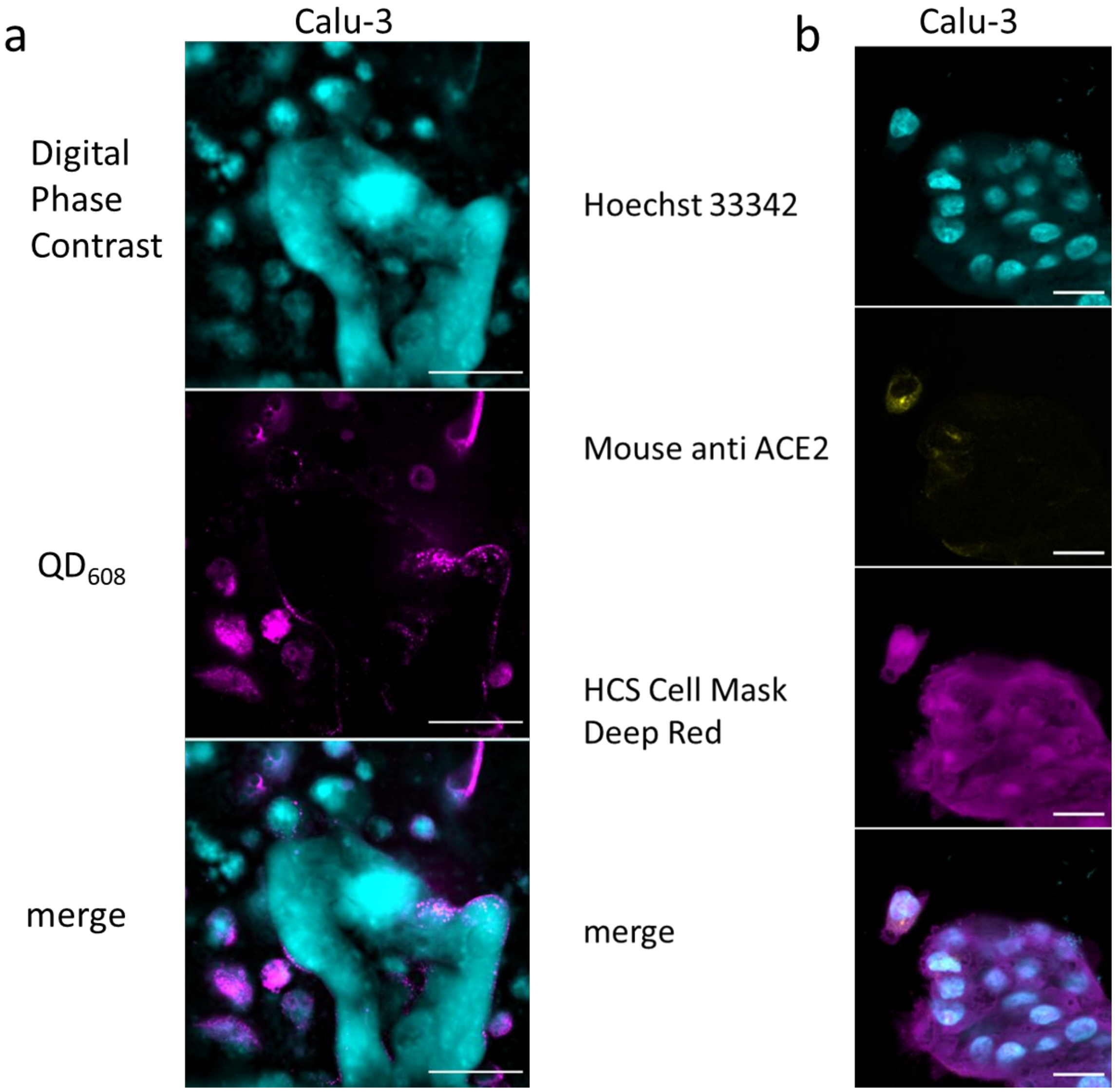

Supplementary Figure 9. Calu-3 epithelial lung cancer cells can internalize QD$_{608}$-RBD. **a,** Representative image montage of Calu-3 treated with 20 nM QD$_{608}$-RBD (magenta) for three hours. Digital Phase Contrast (cyan) was used to visualize cell bodies. 28 μm Z-stack was captured using 14 z-positions 2 μm apart. Scale bar, 50 μm. N = 10 fields from 3 wells. **b,** Representative images of ACE2 immunostaining of Calu-3 cells (yellow) using mouse anti-ACE2 antibody (yellow). Nuclei stained with Hoechst 33342 (cyan) and cell bodies stained with HCS Cell Mask Deep Red (magenta). Scale bar, 25 μm. N = 10 fields each from 3 wells.

Supplementary Videos

Supplementary Video 1 – Confocal timelapse of ACE2-GFP HEK293T treated with Optimem I in the ACE2-GFP channel (yellow). Each frame is 10 minutes for a total of 180 minutes. Scale bar, 25 μm.

Supplementary Video 2 – Confocal timelapse of ACE2-GFP HEK293T treated with 20 nM QD_{608}-RBD in the QD_{608}-RBD channel (magenta). Each frame is 10 minutes for a total of 180 minutes. Scale bar, 25 μm.

Supplementary Video 3 – Confocal timelapse of ACE2-GFP HEK293T treated with 20 nM QD_{608}-RBD in the ACE2-GFP channel (yellow). Each frame is 10 minutes for a total of 180 minutes. Scale bar, 25 μm.

Supplementary Video 4 – Confocal timelapse of ACE2-GFP HEK293T treated with 20 μM Dyngo-4a in the ACE2-GFP channel (yellow). Each frame is 10 minutes for a total of 180 minutes. Scale bar, 25 μm.

Supplementary Video 5 – Confocal timelapse of ACE2-GFP HEK293T treated with 20 nM QD_{608}-RBD and 20 μM Dyngo-4a in the QD_{608}-RBD channel (magenta). Each frame is 10 minutes for a total of 180 minutes. Scale bar, 25 μm.

Supplementary Video 6 – Confocal timelapse of ACE2-GFP HEK293T treated with 20 nM QD_{608}-RBD and 20 μM Dyngo-4a in the ACE2-GFP channel (yellow). Each frame is 10 minutes for a total of 180 minutes. Scale bar, 25 μm.

Supplementary Video 7 – Single molecule imaging timelapse of ACE2-GFP HEK293T treated with 200 pM QD608-RBD in the QD608-RBD channel. Each frame is 20 ms for a total of 20 seconds. Scale bar, 25 μm.

Supplementary References

1. Uddayasankar, U.; Krull, U. J., Energy Transfer Assays Using Quantum Dot–Gold Nanoparticle Complexes: Optimizing Oligonucleotide Assay Configuration Using Monovalently Conjugated Quantum Dots. *Langmuir* **2015,** *31*, 8194-8204.
2. Shang, J.; Ye, G.; Shi, K.; Wan, Y.; Luo, C.; Aihara, H.; Geng, Q.; Auerbach, A.; Li, F., Structural Basis of Receptor Recognition by Sars-Cov-2. *Nature* **2020,** *581*, 221-224.
3. Wang, H.; Yang, P.; Liu, K.; Guo, F.; Zhang, Y.; Zhang, G.; Jiang, C., Sars Coronavirus Entry into Host Cells through a Novel Clathrin- and Caveolae-Independent Endocytic Pathway. *Cell Res.* **2008,** *18*, 290-301.
4. Robertson, M. J.; Deane, F. M.; Robinson, P. J.; Mccluskey, A., Synthesis of Dynole 34-2, Dynole 2-24 and Dyngo 4a for Investigating Dynamin Gtpase. *Nat. Prot.* **2014,** *9*, 851-870.
5. Sigrist, C. J.; Bridge, A.; Le Mercier, P., A Potential Role for Integrins in Host Cell Entry by Sars-Cov-2. *Antivir. Rese.* **2020,** *177*, 104759.
6. Monteil, V.; Kwon, H.; Prado, P.; Hagelkrüys, A.; Wimmer, R. A.; Stahl, M.; Leopoldi, A.; Garreta, E.; Del Pozo, C. H.; Prosper, F., Inhibition of Sars-Cov-2 Infections in Engineered Human Tissues Using Clinical-Grade Soluble Human Ace2. *Cell* **2020**, *181,* 905-913.
7. Tipnis, S. R.; Hooper, N. M.; Hyde, R.; Karran, E.; Christie, G.; Turner, A. J., A Human Homolog of Angiotensin-Converting Enzyme: Cloning and Functional Expression as a Captopril-Insensitive Carboxypeptidase. *J. Biol. Chem*. **2000**, *275*, 33238-33243.
8. Uhlén, M.; Fagerberg, L.; Hallström, B. M.; Lindskog, C.; Oksvold, P.; Mardinoglu, A.; Sivertsson, Å.; Kampf, C.; Sjöstedt, E.; Asplund, A.; Olsson, I.; Edlund, K.; Lundberg, E.; Navani, S.; Szigyarto, C. A.-K.; Odeberg, J.; Djureinovic, D.; Takanen, J. O.; Hober, S.; Alm, T. *et al.* Tissue-Based Map of the Human Proteome. *Science* **2015**, *347*, 1260419.
9. Hikmet F, Méar L, Edvinsson Å, Micke P, Uhlén M, Lindskog C. The Protein Expression

Profile of ACE2 in Human Tissues. *Mol Syst Biol.* **2020**,*16*:e9610.
10. Saheb Sharif-Askari, N.; Saheb Sharif-Askari, F.; Alabed, M.; Temsah, M.-H.; Al Heialy, S.; Hamid, Q.; Halwani, R. Airways Expression of SARS-CoV-2 Receptor, ACE2, and TMPRSS2 Is Lower in Children Than Adults and Increases with Smoking and COPD. *Mol. Ther. Methods Clin. Dev.*, **2020**, 1-6.
11. Oh, E.; Huston, A. L.; Shabaev, A.; Efros, A.; Currie, M.; Susumu, K.; Bussmann, K.; Goswami, R.; Fatemi, F. K.; Medintz, I. L., Energy Transfer Sensitization of Luminescent Gold Nanoclusters: More than Just the Classical Förster Mechanism. *Sci. Rep.* **2016,** *6*, 35538.
12. Förster, T., Zwischenmolekulare Energiewanderung Und Fluoreszenz. *Annalen Der Physik* **1948,** *437*, 55-75.
13. Persson, B., Theory of the Damping of Excited Molecules Located above A Metal Surface. *J. Phys. C: Solid State Phys.* **1978,** *11*, 4251-4269.
14. Persson, B.; Lang, N., Electron-Hole-Pair Quenching of Excited States near a Metal. *Phys. Rev. B* **1982,** *26*, 5409-5415.
15. Lakowicz, J. R., 2.10 Quantum Yield Standars, *Principles of Fluorescence Spectroscopy*. Second Edition; Springer Science & Business Media: New York, 2013; 52-53.
16. Clapp, A. R.; Medintz, I. L.; Mauro, J. M.; Fisher, B. R.; Bawendi, M. G.; Mattoussi, H., Fluorescence Resonance Energy Transfer between Quantum Dot Donors and Dye-Labeled Protein Acceptors. *J. Am. Chem. Soc.* **2004,** *126*, 301-310.
17. Jennings, T. L.; Singh, M. P.; Strouse, G. F., Fluorescent Lifetime Quenching near $d = 1.5$ nm Gold Nanoparticles: Probing Nset Validity. *J. Am. Chem. Soc.* **2006,** *128*, 5462-5467.